RSC Advances




ROYAL SOCIETY OF CHEMISTRY

www.rsc.org/advances

RSC Advances

COMMUNICATION

# Flexible periodical micro- and nano-structuring of stainless steel surface by dual-wavelength double-pulse picosecond laser irradiation

Received 00th January 20xx,
Accepted 00th January 20xx

DOI: 10.1039/x0xx00000x
www.rsc.org/

Mindaugas Gedvilas,*[a] Justinas Mikšys[a] and Gediminas Račiukaitis[a]

**The picosecond laser-induced ripple formation on the stainless steel surface upon irradiation with the linearly-polarized single-pulse and dual-wavelength cross-polarized double-pulse trains in the air was studied experimentally. The characteristic switching of the ripple period and orientation were observed depending on the inter-pulse delay in the dual-wavelength cross-polarized double-pulse train irradiation experiments.**

Birnbaum was the first, who discovered laser-induced periodic surface structures (LIPSS), also known as ripples, on surface of various semiconductors, using a focused ruby laser beam in 1965 [1]. Since that time, the ripples were investigated in numerous scientific works experimentally and theoretically [2-5]. The period of the periodical or quasi-periodical structures is considered one of the most important ripple defining characteristics [5]. There are two main types of the ripples grown after a ultra-short laser irradiation. The coarse or low spatial frequency ripples (LSFR) have a period close to the wavelength of the laser irradiation and direction, perpendicular to the polarization of laser irradiation. The fine or high spatial frequency ripples (HSFR), with a period much smaller than the irradiation wavelength, has direction, parallel to the polarization vector [5]. The most commonly used theoretical model of ripple formation is the interference [6], which states, that ripples are being formed by interference between an incident and the surface scattered light.

These laser induced periodic micro- and nano-ripple structures have found many applications during the last decade. That includes the control of surface wetting [7-9], light extraction and harvesting [10, 11], chemical and mechanical alteration of materials [12], colouring the surfaces [13-16], nano-textured surfaces for bio-sensors [17-19], micro-optical elements [20, 21] and the light absorption enhancement [22-25].

The irradiation with the sequences of the high number of ultra-short laser pulses is required for formation of fine and coarse ripples on a stainless steel surface [26]. Usually, the metal surface is irradiated with the single-pulse trains [27]. However, in some works, double-pulses trains with the same wavelength are being used for the ripple formation [28, 29] and also for laser micro-fabrication [30-33]. In the more complicated approaches, the dual-wavelength double-pulse trains with the time delay in between pulses have been used for various laser processing experiments [34-38]. In the last half-decade, much research on the ripple formation upon the double-pulse femtosecond laser irradiation on silicon and fused silica has been done using parallel- [39-43] and crossed-polarizations [44-46]. There only a few papers dedicated to the laser-induced ripple formation by using the dual-wavelength double-pulsed femtosecond laser irradiation [37, 47] and only two with the crossed-polarizations [45, 48]. However, the time delay between IR and UV pulses was varied only in the range of a few picoseconds [45, 47]. No similar research has been performed on metallic surfaces.

In this work, the experimental results of the picosecond laser-induced ripple formation on the stainless steel surface after irradiation with the linearly-polarized single-pulse trains and dual-wavelength cross-polarized double-pulse trains are presented. The morphology of periodical micro- and nano-ripples was investigated by using a scanning electron microscope (SEM). The periodicity and orientation of structures were analysed by the two-dimensional (2D) Fast Fourier Transformation (FFT). The characteristic coarse or LSFR ripple structures with the wavelength-related periods and the polarization-perpendicular orientations were observed after the single-pulse train irradiation at IR ($\lambda$ = 1064 nm) and UV ($\lambda$ = 355 nm) wavelengths. The ripple period dependence on the laser fluence was found for both single- and double-pulse irradiation regimes. Three distinguishable ranges of the time delays between the IR and UV laser pulses with the characteristic switching of the ripple period and their orientation were found in the dual-wavelength cross-polarized

[a]*Center for Physical Science and Technology, Savanoriu Ave. 231, LT-02300, Vilnius, Lithuania. E-mail: mgedvilas@ftmc.lt*

double-pulse train irradiation experiments. The possible formation mechanisms are discussed.

Stainless steel – grade 304 plates with thickness of 400 µm were chosen as sample material for the laser-induced ripple formation.

The principal scheme of the experimental setup for the dual-wavelength crossed-polarized double-pulse train irradiation is presented in **Fig. 1**. An industrial-grade diode-pumped picosecond laser (Atlantic, Ekspla) with the pulse duration of $\tau = 10$ ps, the repetition rate of $f_{rep} = 100$ kHz and the wavelength of IR irradiation $\lambda = 1064$ nm was used in the experiments. The incident laser light was separated into two beams by the beam splitter cube BSC. The time delay $\Delta t$ between pulses of the fundamental and third harmonics was varied by changing the optical path length of two delay lines DL1 and DL2 with retro-reflection prisms RP1 and RP2, respectively:

$$\Delta t = 2\Delta x / c \qquad (1)$$

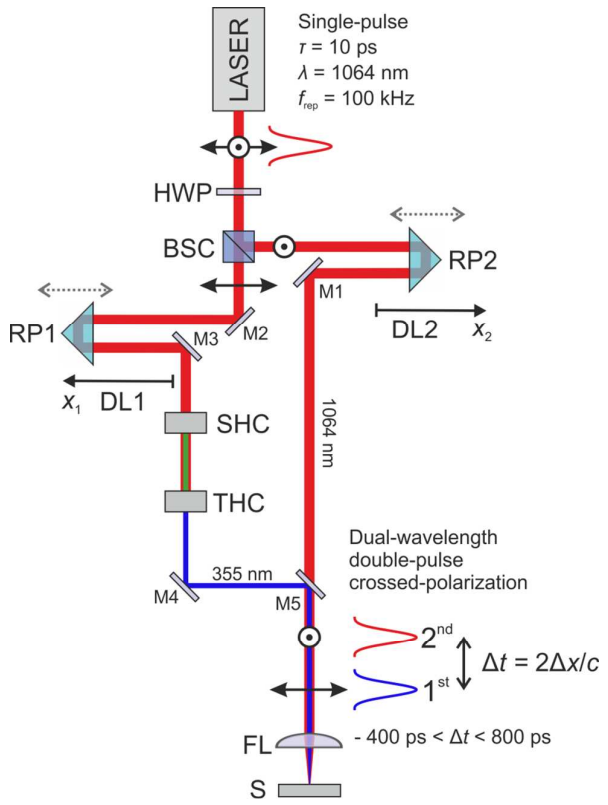


**Fig. 1** Experimental setup for the dual-wavelength (355 nm and 1064 nm) crossed-polarized double-pulse laser irradiation. LASER is a picosecond laser source; BSC is the beam splitter cube, DL1 and DL2 are the delay lines with movable retro-reflection prisms RP1 and RP2; M1, M2, M3, and M4 are the high reflective mirrors; SHC is the second harmonic crystal; THC is the third harmonic crystal; M5 is the harmonic beam splitter mirror; FL is the focusing lens, S is a sample.

where $\Delta x = x_2 - x_1$ is the position difference of the retro-reflector prisms, $x_1$ and $x_2$ are absolute positions of retro-reflection prisms RP1 and RP2, $c = 3.0\times10^8$ m/s is the speed of light in air.

The third harmonics was generated on the left side of the scheme using the second and third harmonics crystals. Both beams were brought together by using the harmonic beam splitter mirror M5 and were focused on the surface of the sample by using the focusing lens FL.

Two regimes of irradiation were used in the experiments: the single-pulse train irradiation and dual-wavelength double-pulse train irradiation (**Fig. 2**). The single-pulse train irradiation was used by using two laser wavelengths: either $\lambda = 1064$ nm (**Fig. 2**a) or $\lambda = 355$ nm (**Fig. 2**b). In the dual-wavelength double-pulse train irradiation scheme, dual-wavelength ($\lambda = 1064$ nm and $\lambda = 355$ nm) pulse pair with the time delay $\Delta t$ between them were used for irradiation of the samples. The negative time delay $\Delta t < 0$ represents the situation when the first pulse was with IR wavelength in the double-pulse pair and UV one was the second (**Fig. 2**c). The positive time delay $\Delta t > 0$ represents the opposite situation when UV pulse is the first in the double-pulse pair and the IR pulse was the second one (**Fig. 2**d). The temporal distance between repetitive laser pulses or double-pulse pairs was $1/f_{rep} = 10$ µs. The number of pulses $N = 1$, 10, 100 and 1000 was used in the irradiation pulse trains.

The laser beam with the Gaussian transverse spatial intensity distribution was used in experiments:

$$F(r) = F_0 \exp\left(-2r^2 / w_0^2\right) \qquad (2)$$

where $F_0$ is the peak laser fluence in the central part of the Gaussian beam, $r$ is the radial distance from the center axis of the beam, $w_0$ is the spot radius on the sample at $1/e^2$ level. The peak laser fluence in the center of the beam was evaluated by $F_0 = 2E_p / (\pi w_0^2)$, where $E_p$ is the laser pulse

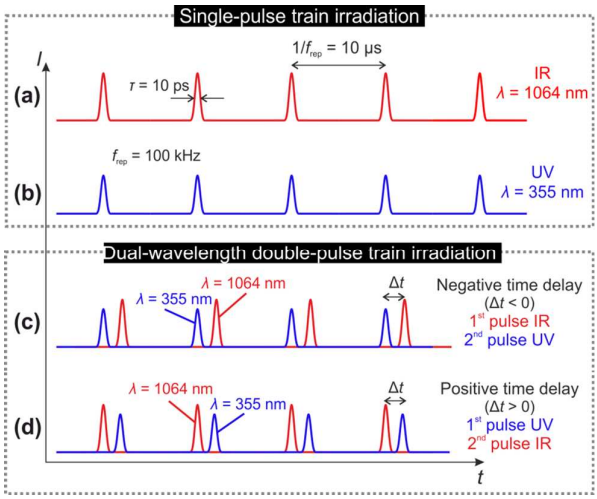


**Fig. 2** Principal scheme of the irradiation schemes, in the intensity versus time representation: (a), (b) - single-pulse train irradiation; (c), (d) - dual-wavelength double-pulse train irradiation.

energy. The peak laser fluence for the IR irradiation was $F_{0\,IR} = 1.1$ J cm$^{-2}$ and for the UV one - $F_{0\,UV} = 0.45$ J cm$^{-2}$. The ripple period was measured across the laser irradiated spot. The radial distance $r$ from the center of the Gaussian beam was converted to the local laser fluence $F(r)$ by using equation (2).

Ripple formation is highly dependent on the number of laser pulses applied to the surface of stainless steel [26, 49]. Usually, the high number of pulses is required for a regular ripple formation using ultra-short laser pulses [26, 27, 50]. In our work, the first experiments were conducted to find the optimal number of laser pulses for the ripple formation in our experimental conditions. The number of laser pulses was changed, keeping the fixed laser fluence at the single-pulse and dual-wavelength cross-polarized double-pulse train irradiation. SEM micrographs of ripples formed using different pulse counts in the irradiation trains and 2D-FFT of the images are given **Fig. 3**. The ripple formation starts after the first 1-10 of laser pulses (**Fig. 3**a, b, c, and f). However, this is the only initial stage of the ripple formation, and the higher contrast image is taken from the experiment with the exposition by $N = 100$ laser pulses (**Fig. 3**c and g). If the exposure time was further increased to the 1000 pulse regime, the unwanted bubbles started to form in the laser processed area for both wavelengths of irradiation (**Fig. 3**d and h).

The main criteria for choosing the optimal processing regime were: the SEM images with the highest possible contrast; characteristic ripple period and their orientation over the main part of the laser spot; the distinguishable and sharp maximum peaks in 2D-FFT of the SEM images. The processing with irradiation exposure using 100 laser pulses was chosen as an optimal number of laser pulses for the further investigations.

The ripple period dependence on the laser fluence was investigated for both single- and double-pulse irradiation experiments. The ripple period was evaluated from 2D-FFT of the SEM micrographs. The free and open source software Gwyddion was used for image analysis and evaluation of the ripple period. 2D-FFT was performed to the SEM micrographs and the ripple period was measured from the

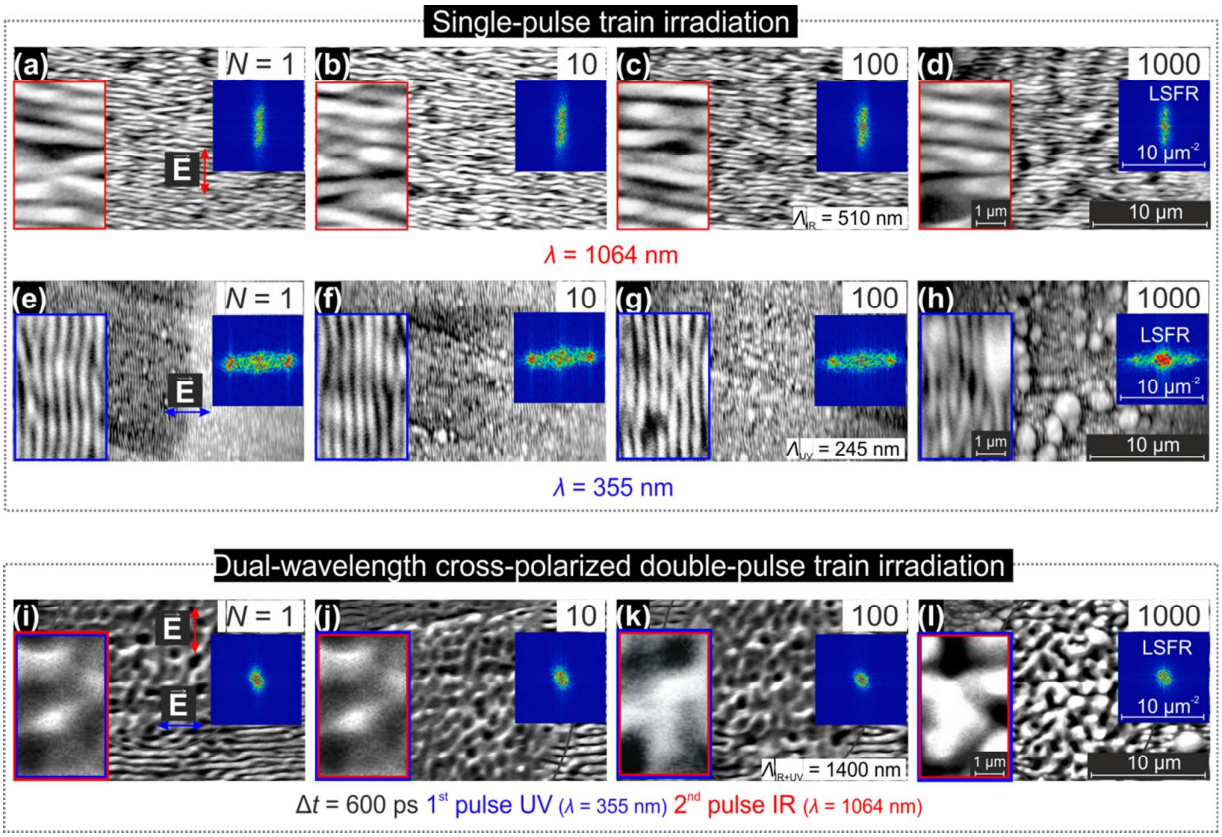


**Fig. 3** SEM micrographs of the ripples formed on the stainless steel surface by the laser irradiation: (a)-(h) single-pulse trains; (i)-(l) dual-wavelength cross-polarized double-pulse trains. The processing parameters: (a)-(d) wavelength of irradiation $\lambda = 355$ nm, laser fluence in the center of the beam $F_{0\,UV} = 0.45$ J cm$^{-2}$; (e)-(h) $\lambda = 1064$ nm, $F_{0\,IR} = 1.1$ J cm$^{-2}$; (i)-(l) time delay $\Delta t = 600$ ps, 1st pulse UV, 2nd pulse IR, laser fluences are same as in (a)-(h). The numbers $N = 1$, 10, 100, 1000 on the top right corners of the images represents the count of laser pulses used in the irradiation trains. The vertical and horizontal arrows in (a), (e) and (i) indicate the orientation of the polarization of the IR and UV laser beams for each row of the images. Inserts on the left bottom corners of the images - four times enlarged micrographs from the center of the pictures. Inserts on the right middle of the micrographs are 2D-FFT of the images. The scale bars, given in (d), (h) and (l), are the same for all images.

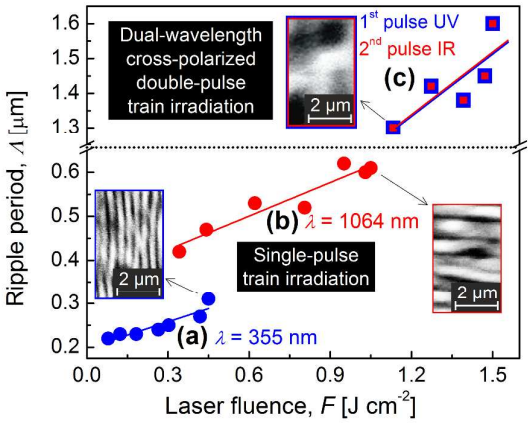


**Fig. 4** The ripple period dependence on the laser fluence. The bottom part of the graph represents the single-pule train irradiation with (a) UV ($\lambda$ = 355 nm); (b) IR ($\lambda$ = 1064 nm) wavelengths. The top part of the graph (c) represents the dual-wavelength cross-polarized double-pulse train irradiation with the time delay of $\Delta t$ = 600 ps between the UV and IR pulses. The number of laser pulses in trains $N$ = 100. The inserts are SEM micrographs of the laser-induced ripples.

distance between the peaks in the spatial frequency domain. The dependence of the ripple period on the laser fluence for the single-pulse and dual-wavelength double-pulse train irradiation is given in **Fig. 4**. The ripple period grows linearly from 215 nm to 310 nm with the increasing laser fluence from 0.05 J cm$^{-2}$ to 0.45 J cm$^{-2}$ applied for the 355 nm wavelength irradiation (**Fig. 4**a). The ripple period linearly grows from 420 nm to 620 nm with the increasing laser fluence from 0.25 J cm$^{-2}$ to 1.05 J cm$^{-2}$ applied for the 1064 nm wavelength irradiation (**Fig. 4**b). The ripple period also grows linearly from 1.3 μm to 1.6 μm with the increasing laser fluence from 1.1 J cm$^{-2}$ to 1.5 J cm$^{-2}$ applied for the dual-wavelength (UV and IR) cross-polarized double-pulse train irradiation with the inter-pulse time delay of $\Delta t$ = 600 ps (**Fig. 4**c).

The mechanism for self-formation of periodic grating structures on a metal surface by an ultra-short laser pulses has been proposed by S. Sakabe et al. [51-53]. The parametric process involving the interaction of laser light and surface plasma waves, as well as the excitation of surface solid-state plasma, suggesting the the increase of ripple period $\Lambda$ with the laser fluence within the range between 0.5$\lambda$ and 0.85$\lambda$ was demonstrated theoretically and experimentally. In our case the ripple periods $\Lambda_{UV}$ and $\Lambda_{IR}$ increased with the laser fluence within the range from 0.62$\lambda_{UV}$ to 0.87$\lambda_{UV}$ and from 0.39$\lambda_{IR}$ to 0.58$\lambda_{IR}$ for the 355 nm and 1064 nm wavelengths of irradiation, respectively. Our experimental results are consistent with this model.

SEM images of the laser-irradiated areas with the dual-wavelength cross-polarized double-pulse trains are presented in **Fig. 5**. The regular ripples were formed on the steel surface that was firstly irradiated by the IR pulse and after 360 ps by the UV pulse (negative time delay $\Delta t$ = - 360 ps) (**Fig. 5**a). The ripple period was $\Lambda$ = 850 nm. **Fig. 5**b shows the sample surface that firstly interacted with the UV pulse, and after the positive time delay of $\Delta t$ = 30 ps, with the IR pulse. The period of ripples, in this case, was $\Lambda$ = 690 nm. The anti-clockwise inclination of ripple orientation by an angle of ~ 14 deg after the switching from negative to positive time delays was observed. The similar rotation of the grating direction in the dual-wavelength cross-polarization irradiation experiments on semiconductor surface depending on the pulse energy ratio between the IR and UV pulses has been observed by T. Q. Jia et al. [37]. The rotation of ripple orientation with the increase of the UV pulse energy was observed at zero delay time between pulses. The rotation in our experiment might be related to interaction of surface plasma waves induced by the electrical field of IR and UV laser beams. **Fig. 5**c shows the quasi-periodical ripple formation with the period of $\Lambda$ = 1.4 μm when the IR beam reached the sample the

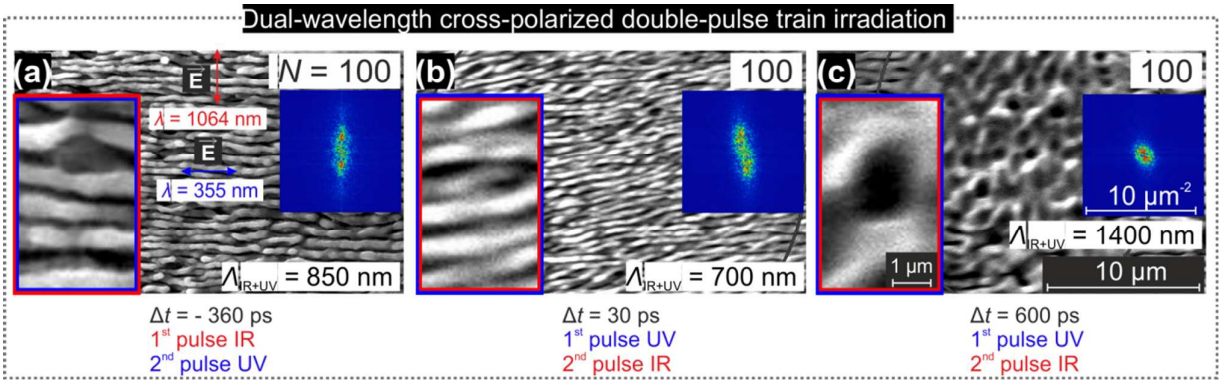


**Fig. 5** SEM micrographs of the stainless steel surface irradiated with the dual-wavelength (1064 nm and 355 nm) cross-polarized double-pulse train at different time delays between the laser pulses: (a) - 1st pulse IR (1064 nm), 2nd pulse UV (355 nm), time delay $\Delta t$ = -360 ps, the ripple period $\Lambda \approx$ 850 nm; (b) - 1st pulse UV, 2nd pulse IR, time delay $\Delta t$ = 30 ps, the ripple period $\Lambda \approx$ 700 nm; (c) - 1st pulse UV, 2nd pulse IR time delay $\Delta t$ = 600 ps, quasi-periodical ripple formation with period $\Lambda$ = 1.4 μm. The number of pulses $N$ = 100 used in irradiation trains, laser fluence in the central area of micrographs: $F_{0\,UV}$ = 0.45 J cm$^{-2}$; $F_{0\,IR}$ = 1.1 J cm$^{-2}$. Inserts on the left of the images - four times enlarged micrographs from the center of the picture. Inserts on the right middle of the micrographs are 2D-FFT of the images. The scale bars on (c) are the same for all images.

second after a time delay of $\Delta t = 600$ ps. The dependence of the ripple period on the time delay between the third and fundamental harmonics is given in **Fig. 6.**

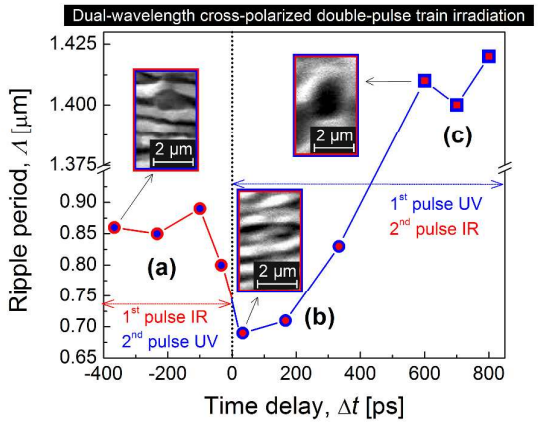


**Fig. 6** The ripple period dependence on the time delay between the IR and UV laser pulses. The experimental points (a) on the left side of the graph is for the case when IR laser pulse reaches the sample surface the first. The points (b) on the central part of the graph represent the case when UV laser pulse reaches the sample surface the first. The points (c) on the right side of the graph are the quasi-periodical ripple formation when $\Delta t$ > 400 ps. The inserts are SEM micrographs of the laser-induced ripples.

The characteristic coarse ripple formation with the wavelength-related periods and polarization-perpendicular orientations was observed when single-pulse trains were applied to the stainless steel surface at the 1064 nm and 355 nm wavelengths of irradiation. The ripple period linearly increased with the applied laser fluence for both wavelengths in the single-pulse train irradiation regimes and also in the double-pulse irradiation experiments.

In conclusion, three distinguishable regimes of the periodical and quasi-periodical ripple formation were observed in the dual-wavelength cross-polarized double-pulse train irradiation experiments with different time delays between the UV and IR laser pulses. Characteristic change of the ripple period and their orientation was observed depending on the pulse order in the train. The decrease in the ripple period and anti-clockwise rotation of their orientation was observed when the time delay switched from negative to positive. Switching from the highly-periodical to quasi-periodical ripples was observed with the time delays higher than 600 ps.

## Notes and references

1 M. Birnbaum, *J. Appl. Phys.*, 1965, **36**, 3688-3689.
2 J. Bonse, J. Krüger, S. Höhm and A. Rosenfeld, *J. Laser Appl.*, 2012, **24**, 042006.
3 M. Huang, Y. Cheng, F. Zhao and Z. Xu, *Ann. Phys.*, 2013, **525**, 74-86.
4 A. Y. Vorobyev and C. Guo, *Laser Photonics Rev.*, 2013, **7**, 385-407.
5 R. Buividas, M. Mikutis and S. Juodkazis, *Progr. Quant. Electron.*, 2014, **38**, 119-156.
6 J. E. Sipe, J. F. Young, J. S. Preston and H. M. van Driel, *Phys. Rev. B*, 1983, **27**, 1141-1154.
7 M. Silvennoinen, J. Kaakkunen, K. Paivasaari, P. Vahimaa and T. Jaaskelainen, *J. Laser Micro Nanoeng.*, 2010, **5**, 97-98.
8 L. Zhang, X. W. Cao, R. Y. Xiang, S. G. Li, L. Wang and H. C. Sun, *Adv. Mater. Res.*, 2014, **1004-1005**, 1311-1315.
9 V. Zorba, L. Persano, D. Pisignano, A. Athanassiou, E. Stratakis, R. Cingolani, P. Tzanetakis and C. Fotakis, *Nanotechnol.*, 2006, **17**, 3234–3238.
10 A. Y. Vorobyev, V. S. Makin and C. Guo, *Phys. Rev. Lett.*, 2009, **102**, 234301.
11 V. Zorba, P. Tzanetakis, C. Fotakis, E. Spanakis, E. Stratakis, D. G. Papazoglou and I. Zergioti, *Appl. Phys. Lett.*, 2006, **88**, 081103.
12 X. Yu, Y. Liao, F. He, B. Zeng, Y. Cheng, Z. Xu, K. Sugioka and K. Midorikawa, *J. Appl. Phys.*, 2011, **109**, 053114.
13 B. Dusser, Z. Sagan, H. Soder, N. Faure, J. P. Colombier, M. Jourlin and E. Audouard, *Opt. Express*, 2010, **18**, 2913-2924.
14 J. Yao, C. Zhang, H. Liu, Q. Dai, L. Wu, S. Lan, A. V. Gopal, V. A. Trofimov and T. M. Lysak, *Appl. Surf. Sci.*, 2012, **258**, 7625-7632.
15 A. Y. Vorobyev and C. Guo, *Appl. Phys. Lett.*, 2008, **92**, 041914.
16 J. Long, P. Fan, M. Zhong, H. Zhang, Y. Xie and C. Lin, *Appl. Surf. Sci.*, 2014, **311**, 461-467.
17 R. Buividas, P. R. Stoddart and S. Juodkazis, *Ann. Phys.*, 2012, **524**, L5-L10.
18 C.-H. Lin, L. Jiang, Y.-H. Chai, H. Xiao, S.-J. Chen and H.-L. Tsai, *Opt. Express*, 2009, **17**, 21581-21589.
19 E. D. Diebold, N. H. Mack, S. K. Doorn and E. Mazur, *Langmuir*, 2009, **25**, 1790-1794.
20 M. Beresna, M. Gecevičius, P. G. Kazansky and T. Gertus, *Appl. Phys. Lett.*, 2011, **98**, 201101.
21 E. Brasselet, G. Gervinskas, G. Seniutinas and S. Juodkazis, *Phys. Rev. Lett.*, 2013, **111**, 193901.
22 P. Gečys, A. Vinčiūnas, M. Gedvilas, A. Kasparaitis, R. Lazdinas and G. Račiukaitis, *J. Laser Micro Nanoeng.*, 2015, **10**, 129-133.
23 A. Žukauskas, M. Malinauskas, A. Kadys, G. Gervinskas, G. Seniutinas, S. Kandasamy and S. Juodkazis, *Opt. Express*, 2013, **21**, 6901-6909.
24 A. Y. Vorobyev, A. N. Topkov, O. V. Gurin, V. A. Svich and C. Guo, *Appl. Phys. Lett.*, 2009, **95**, 121106.
25 T. Y. Hwang, A. Y. Vorobyev and C. Guo, *Opt. Express*, 2011, **19**, A824-A829.
26 B. Liu, W. Wang, G. Jiang, X. Mei, K. Wang, J. Wang and Z. Wang, *J. Laser Appl.*, 2014, **26**, 012001.

27 X. Jun, W. Feng, J. Lan, Z. Liangliang and L. Yongfeng, *Laser Phys.*, 2015, **25**, 056103.

28 V. Hommes, M. Miclea and R. Hergenröder, *Appl. Surf. Sci.*, 2006, **252**, 7449-7460.

29 J. Kim, S. Na, S. Cho, W. Chang and K. Whang, *Optics and Lasers in Engineering*, 2008, **46**, 306-310.

30 A. C. Forsman, P. S. Banks, M. D. Perry, E. M. Campbell, A. L. Dodell and M. S. Armas, *J. Appl. Phys.*, 2005, **98**, 033302.

31 K. Sugioka, M. Iida, H. Takai and K. Micorikawa, *Opt. Lett.*, 2011, **36**, 2734-2736.

32 S. Wu, D. Wu, J. Xu, Y. Hanada, R. Suganuma, H. Wang, T. Makimura, K. Sugioka and K. Midorikawa, *Opt. Express*, 2012, **20**, 28893-28905.

33 S. Wu, D. Wu, J. Xu, H. Wang, T. Makimura, K. Sugioka and K. Midorikawa, *Opt. Express*, 2013, **21**, 24049-24059.

34 W. Zhao, W. Wang, X. Mei, G. Jiang and B. Liu, *Opt. Laser Technol.*, 2014, **58**, 94-99.

35 X. Yu, Q. Bian, B. Zhao, Z. Chang, P. B. Corkum and S. Lei, *Appl. Phys. Lett.*, 2013, **102**, 101111.

36 B. Tan, K. Venkatkrishnan, N. R. Sivakumar and G. K. Gan, *Opt. Laser Technol.*, 2003, **35**, 199-202.

37 T. Q. Jia, H. X. Chen, M. Huang, F. L. Zhao, J. R. Qiu, R. X. Li, Z. Z. Xu, X. K. He, J. Zhang and H. Kuroda, *Phys. Rev. B*, 2005, **72**, 125429.

38 M. Sakamoto, T. Tachikawa, M. Fujitsuka and T. Majima, *Chem. Phys. Lett.*, 2006, **420**, 90-94.

39 A. Rosenfeld, M. Rohloff, S. Höhm, J. Krüger and J. Bonse, *Appl. Surf. Sci.*, 2012, **258**, 9233-9236.

40 T. Y. Derrien, J. Krüger, T. Itina, S. Höhm, A. Rosenfeld and J. Bonse, *Appl. Phys. A*, 2014, **117**, 77-81.

41 S. Höhm, A. Rosenfeld, J. Krüger and J. Bonse, *Appl. Surf. Sci.*, 2013, **278**, 7-12.

42 S. Höhm, A. Rosenfeld, J. Krüger and J. Bonse, *J. Appl. Phys.*, 2012, **112**, 014901.

43 M. Barberoglou, D. Gray, E. Magoulakis, C. Fotakis, P. A. Loukakos and E. Stratakis, *Opt. Express*, 2013, **21**, 18501-18508.

44 M. Rohloff, S. K. Das, S. Höhm, R. Grunwald, A. Rosenfeld, J. Krüger and J. Bonse, *J. Appl. Phys.*, 2011, **110**, 014910.

45 S. Höhm, M. Herzlieb, A. Rosenfeld, J. Krüger and J. Bonse, *Opt. Express*, 2015, **23**, 61-71.

46 S. Höhm, M. Rohloff, A. Rosenfeld, J. Krüger and J. Bonse, *Appl. Phys. A*, 2013, **110**, 553-557.

47 S. Höhm, M. Herzlieb, A. Rosenfeld, J. Krüger and J. Bonse, *Appl. Phys. Lett.*, 2013, **103**, 254101.

48 S. Höhm, M. Herzlieb, A. Rosenfeld, J. Krüger and J. Bonse, *Appl. Surf. Sci.*, 2015, **336**, 39-42.

49 J.-W. Yao, C.-Y. Zhang, H.-Y. Liu, Q.-F. Dai, L.-J. Wu, S. Lan, A. V. Gopal, V. A. Trofimov and T. M. Lysak, *Opt. Express*, 2012, **20**, 905-911.

50 L. Qi, K. Nishii and Y. Namba, *Opt. Lett.*, 2009, **34**, 1846-1848.

51 S. Sakabe, M. Hashida, S. Tokita, S. Namba and K. Okamuro, *Phys. Rev. B*, 2009, **79**, 033409.

52 S. Sakabe, M. Hashida, S. Tokita, S. Namba and K. Okamuro, *Phys. Rev. B*, 2015, **91**, 159902.

53 M. Hashida, Y. Ikuta, Y. Miyasaka, S. Tokita and S. Sakabe, *Appl. Phys. Lett.*, 2013, **102**, 174106.